Simulation of surface plasmon resonance of metallic nanoparticles by the boundary-element method

Jiunn-Woei Liaw

Materials Research Laboratories, Industrial Technology Research Institute, Building 52, 195 Chung-Hsing Road, Section 4, Chutung, Hsinchu 310, Taiwan, China

Received March 7, 2005; revised manuscript received June 2, 2005; accepted June 13, 2005

A set of new surface integral equations (Fredholm equations of the second kind) has been systematically derived from the Stratton–Chu formulation of Maxwell's equations for a two-dimensional TM mode to investigate the interactions of an incident electromagnetic wave with nanostructures, especially metals. With these equations, the surface components (the tangential magnetic field, the normal displacement, and the tangential electric field) on the boundary are solved simultaneously by the boundary-element method numerically. For nanometer-sized structures (e.g., dimension of 10 nm), our numerical results show that surface plasmon resonance causes a strong near-field enhancement of the electric field within a shallow region close to the interface of metal and dielectric. In addition, the corresponding pattern of the far-field scattering cross section is like a dipole. For the submicrometer-sized cases (dimension of several hundreds of nanometers), the numerical results indicate the existence of a standing wave on the backside surface of metals. This phenomenon could be caused by two surface plasmon waves that creep along the contour of metals clockwise and counterclockwise, respectively, and interfere with each other. © 2006 Optical Society of America

OCIS codes: 050.1950, 050.1960, 240.6680, 260.2110, 290.5850.

1. INTRODUCTION

Because of the free electrons of metals, the real part of the permittivity (dielectric constant) of metals normally exhibits a negative value in a certain range of UV to near IR. This unique property causes a surface plasmon resonance (SPR), a collective electron oscillation in the surface of metals, by illuminating light upon the metals if certain conditions are satisfied. Because of the significant near-field enhancement of the electric field, SPR has recently drawn more attention on the applications of near-field optics[1] and the enhancement of spontaneous emission.[2] Numerous new research topics on plasmons have been raised during the past decade. A typical topic is focused on the interaction of light with metallic nanoparticles and its near-field enhancement.[3] An important application is in surface-enhanced Raman spectroscopy. Another interesting topic is the study of metallic film with arrays of subwavelength holes or corrugations that can manipulate the transmission of light.[1,4,5] Other research has investigated plasmonic waveguides, including the nanowire[6–8] and nanoparticle array.[9] Utilizing the nanometer-scaled metal–dielectric composite, the plasmon mode can be used to implement left-handed materials.[10] To simulate the behavior of plasmons and to design plasmonic devices, several numerical methods were developed and adopted. The finite-difference time-domain method (FDTD) has usually been used for SPR analysis.[9] The discrete-dipole approximation, employing intersecting effective spheres, was utilized to analyze the surface plasmon polariton of a nanoneedle.[10] Volume-integral equations in terms of a dyadic Green's tensor were developed for SPR calculation.[7,11–13] The other technique, the multiple multipole method, was also utilized to calculate SPR.[14] Recently, the boundary-element method (BEM) was adopted for two-dimensional (2D)[15] and three-dimensional (3D)[4,16] plasmon modeling because of its advantage of meshing only the boundary. Moreover, the BEM was used to study the second-harmonic generation of 2D problems by consideration of the nonlinear polarization from the fundamental frequency.[17]

In this paper, a set of new formulations of surface integral equations (Fredholm equations of the second kind) is developed for the 2D simulation of light interacting with metallic nanoparticles and are solved by the BEM. These coupled surface integral equations are derived from the Stratton–Chu formula[18] for a 2D TM mode (p polarization). The advantage of the surface integral equations is to reduce the spatial dimension of the problem by one. With these equations, the normal displacement, the tangential electric field, and the tangential magnetic field on the boundary are solved simultaneously. As compared with other BEM studies[15,17,19–21] of the TM mode, our approach calculates these physical components directly, instead of the tangential magnetic field and its normal gradient. In addition, this approach, based on the Stratton–Chu formulation, can be extended straightforward to a 3D problem, unlike the other BEM that uses Debye potentials.[22] Since only the boundaries enclosing different mediums are discretized, fewer meshes are needed than in the other methods that are implemented by the domain mesh, e.g., FDTD, finite-element method, the volume-integral equations method with a dyadic Green's tensor, etc. Because most of the energy of the plasmon is confined within a shallow area close to the interface of metals and dielectrics, the BEM has the advantage in that it calculates the predominant field components along the boundary instead of the domain fields. This unique feature allows the BEM to consume less CPU time and memory for calculation.

2. INTEGRAL PRESENTATIONS

For a 2D TM-mode problem, the electric field is $\mathbf{E}=E_x\mathbf{e}_x+E_y\mathbf{e}_y$ and the magnetic field is $\mathbf{H}=H_z\mathbf{e}_z$. The configuration of an incident p-polarized electromagnetic (EM) wave illuminating upon a scatterer with an incident angle θ_i is depicted in Fig. 1, where the domain Ω_1 (exterior) is an infinite dielectric material with boundary $S\cup S_\infty$ and the domain Ω_2 (interior) is a metal with boundary S. The permittivity (dielectric constant) of the material is denoted by ϵ and the permeability is denoted by μ. On the basis of the Stratton–Chu formulation, the surface integral representations of the electric field and magnetic field in the interior Ω_2 for a 2D TM-mode problem are derived as

$$H_z(\mathbf{x})=\int_S H_z(\mathbf{x}')\mathbf{n}'\cdot\nabla' G_2 \mathrm{d}l' + i\omega\int_S \epsilon_2 E_t(\mathbf{x}')G_2\mathrm{d}l', \quad \mathbf{x}\in\Omega_2, \tag{1}$$

$$\mathbf{E}(\mathbf{x})=i\omega\int_S \mu_2 G_2 H_z \mathrm{d}\mathbf{l}' + \frac{1}{\epsilon_2}\int_S D_n\nabla' G_2\mathrm{d}l' - \int_S E_t\mathbf{e}_z\times\nabla' G_2\mathrm{d}l', \quad \mathbf{x}\in\Omega_2, \tag{2}$$

where

$$G_2=\frac{i}{4}H_0^{(1)}(k_2 r). \tag{3}$$

Since for the TM-mode problem H_z satisfies the scalar Helmholtz equation, Eq. (1) can also be directly derived by Green's theorem.[15,17,19–21] The Green's functions G_2, the singular solution of the Helmholtz equation of medium 2, satisfies

$$\nabla^2 G_2+\omega^2\epsilon_2\mu_2 G_2=-\delta(\mathbf{x}-\mathbf{x}'), \tag{4}$$

where $\delta(\mathbf{x}-\mathbf{x}')$ denotes the Dirac delta function. In Eq. (3), $H_0^{(1)}$ is the Hankel function of the first kind of order zero for the Green's function G_2. The above representations, Eqs. (1) and (2), in terms of the boundary components (the tangential magnetic field H_z, the normal electrical displacement D_n, and the tangential electrical field E_t) can be used to calculate the field in domain Ω_2, once these boundary components are solved. At the boundary S, the values of (H_z, D_n, E_t) satisfy the continuity conditions for the interior and exterior materials, where $\mathbf{e}_z$ is the unit vector of the z direction, the unit normal vector $\mathbf{n}$ is in the inner direction, and the unit tangential vector is defined as $\mathbf{t}=\mathbf{n}\times\mathbf{e}_z$. The wavenumbers k_j, $j=1,2$, are of medium 1 and 2, respectively. For the exterior field, the solution can be decomposed of two parts: one is the incident part and the other is the scattering part. The total fields in domain Ω_1 are the sum of the incident field and the scattering field: $\mathbf{E}=\mathbf{E}^i+\mathbf{E}^s$, $H_z=H_z^i+H_z^s$. The superscript i represents the incident part and the superscript s represents the scattering part. The incident part satisfies Maxwell's equations of medium 1 in an infinite homogeneous domain without the obstacle. However, the scattering field, regarded as a secondary source radiating from the boundary S, also satisfies Maxwell's equations of medium 1 in domain Ω_1. Since the scattering field must satisfy the Sommerfeld radiation condition at S_∞, the surface integral representations of the electric field and magnetic field of the scattering part in exterior Ω_1 are expressed as

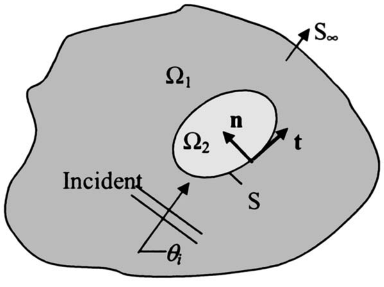

Fig. 1. Configuration of a plane p-polarized EM wave illuminating on a scatterer Ω_2 in an infinite domain Ω_1 with an incident angle θ_i

$$H_z^s(\mathbf{x})=-\int_S H_z^s(\mathbf{x}')\mathbf{n}'\cdot\nabla' G_1\mathrm{d}l' - i\omega\int_S \epsilon_1 E_t^s(\mathbf{x}')G_1\mathrm{d}l', \quad \mathbf{x}\in\Omega_1, \tag{5}$$

$$\mathbf{E}^s(\mathbf{x})=-i\omega\int_S \mu_1 G_1 H_z^s\mathrm{d}\mathbf{l}' - \frac{1}{\epsilon_1}\int_S D_n^s\nabla' G_1\mathrm{d}l' + \int_S E_t^s\mathbf{e}_z\times\nabla' G_1\mathrm{d}l', \quad \mathbf{x}\in\Omega_1, \tag{6}$$

where

$$G_1=\frac{i}{4}H_0^{(1)}(k_1 r). \tag{7}$$

In Eq. (7), $H_0^{(1)}$ is the Hankel functions of the first kind of order zero for the Green's function G_1 to satisfy the outgoing wave behavior in the far field because of the time-harmonic factor $\exp(-i\omega t)$. The Green's function G_1, the singular solution of the Helmholtz equation of medium 1, satisfies

$$\nabla^2 G_1+\omega^2\epsilon_1\mu_1 G_1=-\delta(\mathbf{x}-\mathbf{x}'). \tag{8}$$

Consider an incident wave propagating in a homogeneous medium of material 1; the incident parts in the area of interior Ω_2 satisfy

$$H_z^i(\mathbf{x})=\int_S H_z^i(\mathbf{x}')\mathbf{n}'\cdot\nabla' G_1\mathrm{d}l' + i\omega\int_S \epsilon_1 E_t^i(\mathbf{x}')G_1\mathrm{d}l', \quad \mathbf{x}\in\Omega_2, \tag{9}$$

$$\mathbf{E}^i(\mathbf{x}) = i\omega\int_S \mu_1 G_1 H_z^i \mathrm{d}\mathbf{l}' + \frac{1}{\epsilon_1}\int_S D_n^i \nabla' G_1 \mathrm{d}l' - \int_S E_t^i \mathbf{e}_z \times \nabla' G_1 \mathrm{d}l', \quad \mathbf{x} \in \Omega_2. \qquad (10)$$

The above equations are identities, which are auxiliary equations for the following derivation of the integral equations of the total field of exterior Ω_1.

3. SURFACE INTEGRAL EQUATIONS

A governing equation of the unknowns (H_z, D_n, E_t) is further derived from Eq. (1) by letting the observation point $\mathbf{x}$ approach $\mathbf{x}_0$ of the surface $S(\mathbf{x}_0 \in S)$.

$$\frac{1}{2}H_z(\mathbf{x}_0) = \int_S H_z(\mathbf{x}')\mathbf{n}' \cdot \nabla' G_2 \mathrm{d}l' + i\omega\int_S E_t(\mathbf{x}')\epsilon_2 G_2 \mathrm{d}l', \quad \mathbf{x}_0 \in S. \qquad (11)$$

The first integral on the right-hand side of Eq. (11) is in the sense of a Cauchy principal value. By taking the inner product of Eq. (2) with $\epsilon_2\mathbf{n}(\mathbf{x}_0)$, where $\mathbf{x}_0 \in S$, and then letting $\mathbf{x} \to \mathbf{x}_0$, we can obtain another integral equation as

$$\frac{1}{2}D_n(\mathbf{x}_0) = i\omega\int_S \epsilon_2\mu_2 G_2 H_z \mathbf{n}(\mathbf{x}_0) \cdot \mathrm{d}\mathbf{l}' + \int_S D_n \mathbf{n}(\mathbf{x}_0) \cdot \nabla' G_2 \mathrm{d}l' - \int_S \epsilon_2 E_t \mathbf{n}(\mathbf{x}_0) \cdot \mathbf{e}_z \times \nabla' G_2 \mathrm{d}l', \quad \mathbf{x}_0 \in S. \qquad (12)$$

The second integral on the right-hand side of Eq. (12) is in the sense of a Cauchy principal value. Using the same approach but taking the inner product of Eq. (2) with $\mathbf{t}(\mathbf{x}_0)$, where $\mathbf{x}_0 \in S$, and letting $\mathbf{x} \to \mathbf{x}_0$, the other integral equation is also obtained as

$$\frac{1}{2}E_t(\mathbf{x}_0) = i\omega\int_S \mu_2 G_2 H_z \mathbf{t} \cdot \mathrm{d}\mathbf{l}' + \frac{1}{\epsilon_2}\int_S D_n \mathbf{t} \cdot \nabla' G_2 \mathrm{d}l' - \int_S E_t \mathbf{t} \cdot \mathbf{e}_z \times \nabla' G_2 \mathrm{d}l', \quad \mathbf{x}_0 \in S. \qquad (13)$$

The third integral on the right-hand side of Eq. (13) is in the sense of a Cauchy principal value. Equations (11)–(13), derived from the aspect of interior Ω_2, are valid for $\forall \mathbf{x}_0 \in S$. For the sake of simplicity, we use $\mathbf{x}$ to replace $\mathbf{x}_0$ in the following. Using the same procedure of obtaining the integral equations for interior Ω_2, we derive the integral equations of the scattering part of the exterior Ω_1 from Eqs. (5) and (6) as

$$\frac{1}{2}H_z^s(\mathbf{x}) = -\int_S H_z^s(\mathbf{x}')\mathbf{n}' \cdot \nabla' G_1 \mathrm{d}l' - i\omega\int_S E_t^s(\mathbf{x}')\epsilon_1 G_1 \mathrm{d}l', \quad \mathbf{x} \in S, \qquad (14)$$

$$\frac{1}{2}D_n^s = -i\omega\int_S H_z^s \epsilon_1\mu_1 G_1 \mathbf{n} \cdot \mathrm{d}\mathbf{l}' - \int_S D_n^s \mathbf{n} \cdot \nabla' G_1 \mathrm{d}l' + \int_S \epsilon_1 E_t^s \mathbf{n} \cdot \mathbf{e}_z \times \nabla' G_1 \mathrm{d}l', \quad \mathbf{x} \in S, \qquad (15)$$

$$\frac{1}{2}E_t^s = -i\omega\int_S \mu_1 G_1 H_z^s \mathbf{t} \cdot \mathrm{d}\mathbf{l}' - \frac{1}{\epsilon_1}\int_S D_n^s \mathbf{t} \cdot \nabla' G_1 \mathrm{d}l' + \int_S E_t^s \mathbf{t} \cdot \mathbf{e}_z \times \nabla' G_1 \mathrm{d}l', \quad \mathbf{x} \in S. \qquad (16)$$

Furthermore, taking into account the incident part, the identity formulas are also obtained through the same manipulations:

$$\frac{1}{2}H_z^i(\mathbf{x}) = \int_S H_z^i(\mathbf{x}')\mathbf{n}' \cdot \nabla' G_1 \mathrm{d}l' + i\omega\int_S E_t^i(\mathbf{x}')\epsilon_1 G_1 \mathrm{d}l', \quad \mathbf{x} \in S, \qquad (17)$$

$$\frac{1}{2}D_n^i = i\omega\int_S H_z^i \epsilon_1\mu_1 G_1 \mathbf{n} \cdot \mathrm{d}\mathbf{l}' + \int_S D_n^i \mathbf{n} \cdot \nabla' G_1 \mathrm{d}l' - \int_S \epsilon_1 E_t^i \mathbf{n} \cdot \mathbf{e}_z \times \nabla' G_1 \mathrm{d}l', \quad \mathbf{x} \in S, \qquad (18)$$

$$\frac{1}{2}E_t^i = i\omega\int_S \mu_1 G_1 H_z^i \mathbf{t} \cdot \mathrm{d}\mathbf{l}' + \frac{1}{\epsilon_1}\int_S D_n^i \mathbf{t} \cdot \nabla' G_1 \mathrm{d}l' - \int_S E_t^i \mathbf{t} \cdot \mathbf{e}_z \times \nabla' G_1 \mathrm{d}l', \quad \mathbf{x} \in S. \qquad (19)$$

Combining Eq. (14) with (17), Eq. (15) with (18), and Eq. (16) with (19), a set of integral equations of the total field of the exterior Ω_1 is obtained as

$$\frac{1}{2}H_z(\mathbf{x}) = H_z^i - \int_S H_z(\mathbf{x}')\mathbf{n}' \cdot \nabla' G_1 \mathrm{d}l' - i\omega\int_S E_t(\mathbf{x}')\epsilon_1 G_1 \mathrm{d}l', \quad \mathbf{x} \in S, \qquad (20)$$

$$\frac{1}{2}D_n = D_n^i - i\omega\int_S H_z \epsilon_1\mu_1 G_1 \mathbf{n} \cdot \mathrm{d}\mathbf{l}' - \int_S D_n \mathbf{n} \cdot \nabla' G_1 \mathrm{d}l' + \int_S \epsilon_1 E_t \mathbf{n} \cdot \mathbf{e}_z \times \nabla' G_1 \mathrm{d}l', \quad \mathbf{x} \in S, \qquad (21)$$

$$\frac{1}{2}E_t = E_t^i - i\omega \int_S \mu_1 G_1 H_z \mathbf{t} \cdot \mathrm{d}\mathbf{l}' - \frac{1}{\epsilon_1}\int_S D_n \mathbf{t} \cdot \nabla' G_1 \mathrm{d}l' + \int_S E_t \mathbf{t} \cdot \mathbf{e}_z \times \nabla' G_1 \mathrm{d}l', \quad \mathbf{x} \in S. \tag{22}$$

Now we have two sets of integral equations, one set, Eqs. (11)–(13), is for the exterior Ω_1, and the other, Eqs. (20)–(22), is for the interior Ω_2. Although the values of (H_z, D_n, E_t) of boundary S satisfy the continuity conditions for the interior and exterior materials, these equations are not independent. We have to choose appropriate equations from them as the governing equations. Since the scattering phenomena result from the nonhomogeneity of materials, we can recombine the two sets of integral equations to exhibit the coupled forms. First, by taking a summation of Eq. (11) with (20), Eq. (12) with (21), and Eq. (13) with (22), we derive a new set of three coupled integral equations with a Cauchy principal value as follows:

$$H_z(\mathbf{x}) = H_z^i(\mathbf{x}) - \int_S H_z(\mathbf{x}')\mathbf{n}' \cdot \nabla'[G_1 - G_2]\mathrm{d}l' - i\omega \int_S E_t(\mathbf{x}') \times [\epsilon_1 G_1 - \epsilon_2 G_2]\mathrm{d}l', \quad \mathbf{x} \in S, \tag{23}$$

$$D_n = D_n^i - i\omega \int_S H_z[\epsilon_1\mu_1 G_1 - \epsilon_2\mu_2 G_2]\mathbf{n} \cdot \mathrm{d}\mathbf{l}' - \int_S D_n \mathbf{n} \cdot \nabla'[G_1 - G_2]\mathrm{d}l' + \int_S E_t \mathbf{n} \cdot \mathbf{e}_z \times \nabla'[\epsilon_1 G_1 - \epsilon_2 G_2]\mathrm{d}l', \tag{24}$$

$$E_t = E_t^i - i\omega \int_S H_z[\mu_1 G_1 - \mu_2 G_2]\mathbf{t} \cdot \mathrm{d}\mathbf{l}' - \int_S D_n \mathbf{t} \cdot \nabla' \left[\frac{G_1}{\epsilon_1} - \frac{G_2}{\epsilon_2}\right]\mathrm{d}l' + \int_S E_t \mathbf{t} \cdot \mathbf{e}_z \times \nabla'[G_1 - G_2]\mathrm{d}l'. \tag{25}$$

Equations (23)–(25) are Fredholm equations of the second kind because the unknowns (H_z, D_n, E_t) exist inside and outside the integrals. Since these integral equations contain only the surface integrals but without the domain integral, they are called the surface integral equations and can be dealt with numerically by the BEM. On the other hand, we can also subtract Eq. (11) from Eq. (20), Eq. (12) from Eq. (21), and Eq. (13) from Eq. (22) to obtain the other set of integral equations of the total field:

$$0 = H_z^i(\mathbf{x}) - \int_S H_z(\mathbf{x}')\mathbf{n}' \cdot \nabla'[G_1 + G_2]\mathrm{d}l' - i\omega \int_S E_t(\mathbf{x}')[\epsilon_1 G_1 + \epsilon_2 G_2]\mathrm{d}l', \quad \mathbf{x} \in S, \tag{26}$$

$$0 = D_n^i - i\omega \int_S H_z[\epsilon_1\mu_1 G_1 + \epsilon_2\mu_2 G_2]\mathbf{n} \cdot \mathrm{d}\mathbf{l}' - \int_S D_n \mathbf{n} \cdot \nabla'[G_1 + G_2]\mathrm{d}l' + \int_S E_t \mathbf{n} \cdot \mathbf{e}_z \times \nabla'[\epsilon_1 G_1 + \epsilon_2 G_2]\mathrm{d}l', \tag{27}$$

$$0 = E_t^i - i\omega \int_S H_z[\mu_1 G_1 + \mu_2 G_2]\mathbf{t} \cdot \mathrm{d}\mathbf{l}' - \int_S D_n \mathbf{t} \cdot \nabla' \left[\frac{G_1}{\epsilon_1} + \frac{G_2}{\epsilon_2}\right]\mathrm{d}l' + \int_S E_t \mathbf{t} \cdot \mathbf{e}_z \times \nabla'[G_1 + G_2]\mathrm{d}l'. \tag{28}$$

Equations (26)–(28) belong to the Fredholm equations of the first kind because the unknowns (H_z, D_n, E_t) exist only inside the integrals. Although the formulations of Eqs. (26)–(28) are correct theoretically, they are not recommended to be used as the governing equations due to the poor numerical stability of Fredholm's first kind. When the problem is dealt with by discretization, the integral equations are transformed into a set of linear algebra equations. Because the diagonal terms of the matrix are small for the first kind, its numerical results are sensitive to the error caused by the discretization, i.e., the matrix is ill-conditioned. In contrast, the diagonal terms of the matrix for the second kind are more dominant than the nondiagonal terms, so its numerical stability is superior to the first kind. Therefore a set of integral equations of Fredholm's second kind, Eqs. (23)–(25), is used as the governing equation for the numerical calculation throughout the paper, in terms of three unknowns (H_z, D_n, E_t). Instead of our solving the three coupled integral equations, an alternative way is to choose a set of surface integral equations, Eqs. (11) and (20), as the governing equations for the two unknowns (H_z, E_t) on the enclosed surface S; this method has been used in some studies.[15,17,19–21] In principle, the two methods should be equivalent. However, for the numerical viewpoint, using Eqs. (11) and (20) has an advantage in that we can construct a smaller matrix of $2n \times 2n$ than the matrix of $3n \times 3n$ by using Eqs. (23)–(25), if the boundary of the scatterer is discretized by n points. This is to say that the new method, with Eqs. (23)–(25), takes more CPU time and memory to obtain and solve the matrix than the method with Eqs. (11) and (20). On the other hand, the new method has the advantage in that we can calculate the surface information (H_z, D_n, E_t) directly, where the normal displacement field D_n, as well as the tangential electric field E_t, are of importance to study plasmon behavior. In contrast, it is difficult to obtain the surface information of D_n by the method of Eqs. (11) and (20); an additional equation is needed from the derivative of Eq. (1), and a numerical difficulty of the hypersingularity of the kernel function needs to be overcome. In addition, Eqs. (11) and (20) are Fredholm's second kind for H_z but Fredholm's first kind for E_t, while Eqs. (23)–(25) are Fredholm's second kind for (H_z, D_n, E_t). Since Fredholm's second kind has better numerical stability than the first kind, it is reasonable to say that the accuracy of the new method could be superior to the method of Eqs. (11) and (20). Moreover, after solving the unknowns (H_z, D_n, E_t) by the new proposed method, we can calculate the field values of $\mathbf{E}=\mathbf{E}^i+\mathbf{E}^s$, $H_z=H_z^i+H_z^s$ (e.g., the near-field distribution) straightforwardly by substituting (H_z, D_n, E_t) into Eqs. (1)–(4).

4. SCATTERING CROSS SECTION

The far-field scattering cross section (SCS) of the TM mode is defined as

$$\sigma(\theta;\theta_i) = \lim_{|\mathbf{x}|\to\infty} 2\pi|\mathbf{x}| \frac{|\mathbf{E}^s \times \bar{\mathbf{H}}^s \cdot \mathbf{e}_r|}{\|\mathbf{E}^i \times \bar{\mathbf{H}}^i\|}$$

$$= \lim_{|\mathbf{x}|\to\infty} 2\pi|\mathbf{x}| \frac{\|\mathbf{E}^s \cdot \mathbf{e}_r\|^2}{\|\mathbf{E}^i\|^2} = \lim_{|\mathbf{x}|\to\infty} 2\pi|\mathbf{x}| \frac{|H_z^s|^2}{|H_z^i|^2}, \quad (29)$$

where $\bar{\mathbf{H}}^s(\mathbf{x})$ is the complex conjugate of $\mathbf{H}^s(\mathbf{x})$, θ is the observing angle, and θ_i is the incident angle. The unit vector $\mathbf{e}_r=\mathbf{x}/|\mathbf{x}|$ is $(\cos\theta, \sin\theta)$. Using the asymptotic form of Hankel's function,

$$H_n^{(1)}(z) \approx \sqrt{\frac{2}{\pi z}} \exp[i(z - n\pi/2 - \pi/4)], \text{ as } |z| \gg 1; \quad (30)$$

and using $r=|\mathbf{x}-\mathbf{x}'| \approx |\mathbf{x}| - \mathbf{x}' \cdot \mathbf{e}_r$ $(|\mathbf{x}| \gg |\mathbf{x}'|, \mathbf{x}' \in S)$, the asymptotic form of Green's function is expressed as

$$G_1(k_1 r) \approx \sqrt{\frac{1}{8\pi k_1 |\mathbf{x}|}} \exp[i(k_1|\mathbf{x}| + \pi/4 - k_1 \mathbf{x}' \cdot \mathbf{e}_r)], \quad \text{as } |\mathbf{x}| \to \infty. \quad (31)$$

Substituting approximation (31) into the integral representations of $\mathbf{E}^s, H_z^s$ and then into Eq. (29), the SCS can be expressed, in terms of the surface components H_z^s, E_t^s, as

$$\sigma(\theta;\theta_i) = \frac{k_1}{4} \left| \int_S \left[-\mathbf{n}' \cdot \mathbf{e}_r \frac{|H_z^s|}{|H_z^i|} + \frac{|E_t^s|}{\|\mathbf{E}^i\|} \right] \exp(-ik_1 \mathbf{x}' \cdot \mathbf{e}r) \mathrm{d}l' \right|^2. \quad (32)$$

According to Eq. (32), the SCS can be calculated, once the surface components H_z^s, E_t^s are solved. Furthermore, the mean SCS, $\bar{\sigma}$, is defined as

$$\bar{\sigma}(\theta_i) = \frac{1}{2\pi} \int_0^{2\pi} \sigma \mathrm{d}\theta, \quad (33)$$

which is a function of the incident angle θ_i.

5. NUMERICAL RESULTS AND DISCUSSION

The surface integral equations of Eqs. (23)–(25) are adopted and dealt with by the BEM because of the superior numerical stability of the Fredholm equations of the second kind. To implement the BEM, a three-node, isoparameter, quadratic element is used to discretize the geometric boundary and the physical unknowns to solve the integral equations of 2D problems. First, the boundary S is divided into several segments, the so-called boundary elements. Each segment is composed of three nodes. The position vector $\mathbf{x}^j$ of any point in the jth element and the corresponding field values (H_z, D_n, E_t) of the point denoted by F^j are interpolated by the nodal values as

$$\mathbf{x}^j(\xi) = \sum_{i=1}^{3} N_i(\xi) \mathbf{x}_i^j, \quad (34)$$

$$F^j(\xi) = \sum_{i=1}^{3} N_i(\xi) F_i^j, \quad (35)$$

where $\mathbf{x}_i^j$ is the ith node of the jth element on the boundary S, and F_i^j is the field value at $\mathbf{x}_i^j$. The shape functions $N_k(\xi), k=1,2,3$, of interpolation of the three-node element are

$$N_1(\xi) = \frac{1}{2}\xi(\xi - 1), \quad (36)$$

$$N_2(\xi) = 1 - \xi^2, \quad (37)$$

$$N_3(\xi) = \frac{1}{2}\xi(\xi + 1), \quad (38)$$

where the local coordinate ξ is defined between −1 and 1 in each element. After the discretization of the boundary, the numerical integrations are fulfilled by using the Gaussian quadrature. Consequently, the surface integral equations are transformed into a set of linear algebraic equations with the unknowns of the nodal values F_i^j. Since the procedure of implementing the BEM is a standard one,[23] no attempt is made to mention it in detail in this paper. However, it is noted that the singularities of Green's functions should be carefully dealt with when the observing point $\mathbf{x}$ and the field point $\mathbf{x}'$ coincide, i.e., as $r=|\mathbf{x}'-\mathbf{x}| \to 0$. Numerical errors are caused by the singularity when the observing point $\mathbf{x}$ is the junction point between the two adjacent segments with different mesh sizes during the integration. This problem can be overcome by a numerical scheme of a Cauchy principal value. It allows us to optimize the distribution of the mesh size flexibly to discretize the boundary. To verify the precision of our BEM program, typical examples were tested: circular silver ($r=10-300$ nm) with relative permittivity $\epsilon_{2r}=(-4.42, 0.73)$ embedded in an unbounded dielectric domain, relative permittivity $\epsilon_{1r}=(1,0)$, and illumination by a plane p-polarized EM wave at an angular frequency $\omega=4.558\times10^{15}$ rad/s (3 eV, $\lambda_0=413$ nm).[24] Comparing the results of the BEM with the analytical solutions, good agreement is obtained (error <0.5%). In addition, the same cases of Ref. 17 (Fig. 12 therein) were calculated by the new surface integral equations, and our results are in accordance with Ref. 17. All the field values in this paper are normalized with the amplitude of the incident field:

$$H_z/|H_z^i|, D_n/\|\epsilon_1 \mathbf{E}^i\|, \quad E_t/\|\mathbf{E}^i\|, \quad \mathbf{E}/\|\mathbf{E}^i\|,$$

where

$$\|\mathbf{E}^i\| = \frac{k_1}{\omega\epsilon_1}|H_z^i|.$$

Consider that the shape of the silver nanoparticle is an ellipse, $(x/a)^2+(y/b)^2=1$, illuminated by light (3 eV) with $\theta_i=0°$. The mean SCS, $\bar{\sigma}$, of different ellipses of silver are depicted against the aspect ratio b/a in Fig. 2 with fixed $a=10$ nm. In these cases, 360 meshes are divided along the contour of the boundary S for discretization. Figure 2 shows that the maximum mean SCS takes place at $b/a=3.8$. The real and imaginary parts of the total field of the normalized values of (H_z,D_n,E_t) on the boundary S are plotted in Figs. 3(a) and 3(b), respectively, for $b/a=3.8$. In this case, $\theta_i=0°$, the polarization of the electric field is parallel to the longest principal axis of the ellipse to cause a strong collective oscillation of electrons along this axis (the so-called SPR). Furthermore, because the characteristic length is smaller than the penetration depth (27.5 nm) of the surface plasmon wave, the electric field inside the nanoparticle is almost uniform; the normalized value of the electric field is around 3 as shown in Fig. 4(a), and the normalized magnetic field is depicted in Fig. 4(b). The SCS in Fig. 4(c) exhibits a dipole behavior ($\bar{\sigma}=176.4$ nm), since the characteristic length of this nanoparticle is much smaller than the wavelength of the illuminating light.

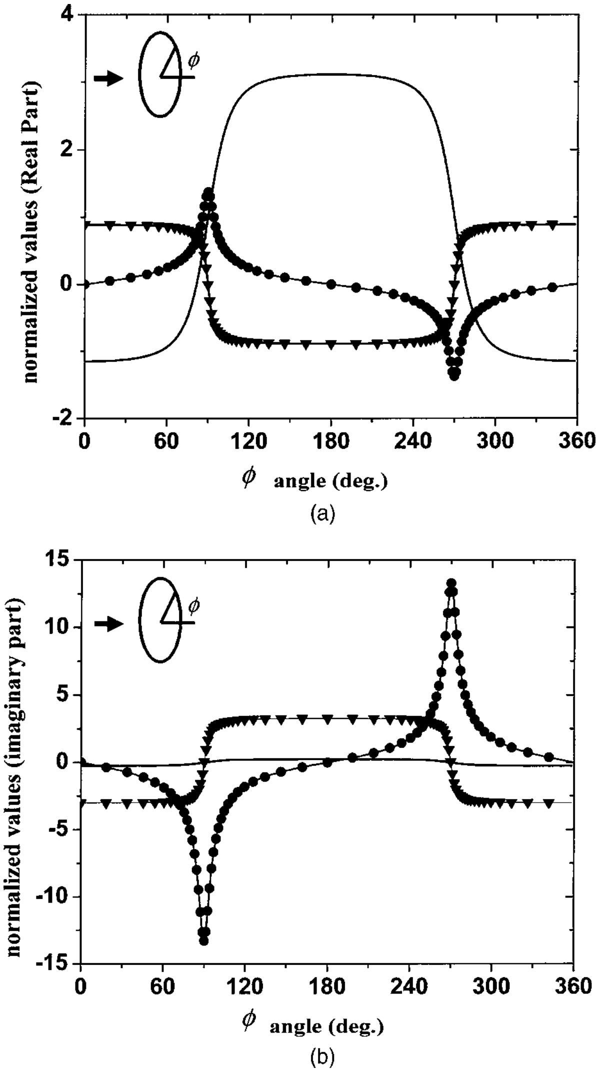

(a)

(b)

Fig. 3. Nanometer-sized elliptical silver ($a=10$ nm, $b=38$ nm) with $\epsilon_{2r}=(-4.42,0.73)$, in air, $\epsilon_{1r}=1$, at $\omega=4.558\times10^{15}$ rad/s (3 eV, $\lambda_0=413$ nm), $\theta_i=0°$. (a) The real parts of the surface components of the total field along the circumference. (b) The imaginary parts. ϕ is the angle of the polar coordinate. Solid curves $H_z/|H_z^i|$; curves with circles, $D_n/\|\epsilon_1\mathbf{E}^i\|$; curves with triangles, $E_t/\|\mathbf{E}^i\|$.

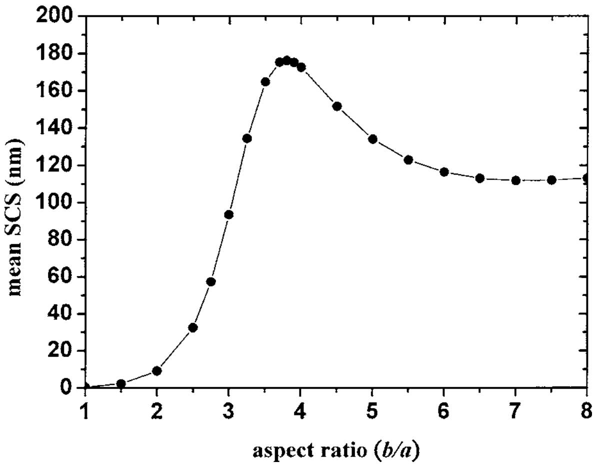

Fig. 2. Mean SCS, $\bar{\sigma}$, versus the aspect ratio b/a for elliptical silver ($a=10$ nm) with $\epsilon_{2r}=(-4.42,0.73)$, in air, $\epsilon_{1r}=1$, at $\omega=4.558\times10^{15}$ rad/s, (3 eV), $\theta_i=0°$.

When the dimensions of metals are in the submicrometer range, the scattering behavior of the metallic particle is different from the nanometer-scaled one. The reason is that the characteristic length is much larger than the penetration depth of the surface plasmon wave. Consider a submicrometer-sized circular silver ($r=400$ nm) with $\epsilon_{2r}=(-4.42,0.73)$, in air, $\epsilon_{1r}=1$, at $\omega=4.558\times10^{15}$ rad/s (3 eV). The distributions of the total field of electric and magnetic fields are depicted in Figs. 5(a) and 5(b), respectively. Obviously, Fig. 5 shows a ripple with nodal points on the backside of the metal. The pattern results from a standing wave caused by two surface plasmon waves creeping along the circumference of metal counterclockwise and clockwise, respectively. It means that when the illuminating light impinges upon the metal, a part of the energy is converted into the surface plasmon waves. The two opposite-directional (counterclockwise and clockwise) surface plasmon waves interfere with each other to generate the standing wave on the surface of the scatterer, especially on the backside. The novel phenomenon is different from the common concept of optical diffraction. Furthermore, because of the shielding effect of metal on the EM field, the incident wave cannot directly transmit throughout the scatterer but can creep along it with a thin penetration depth. Hence the backside of a submicrometer metallic particle is not a shallow zone of a perfect electric conductor. If the radius of curvature of the metallic particle is infinite, its wavenumber k_{sp} can be expressed by a well-known equation,

$$k_{\mathrm{sp}} = k_0\sqrt{\frac{\epsilon_{1r}\epsilon_{2r}}{\epsilon_{1r}+\epsilon_{2r}}}, \tag{39}$$

where $k_0=\omega/c$ and c is the light speed in vacuum.[8] Equation (39) represents the wavenumber of a surface plasmon

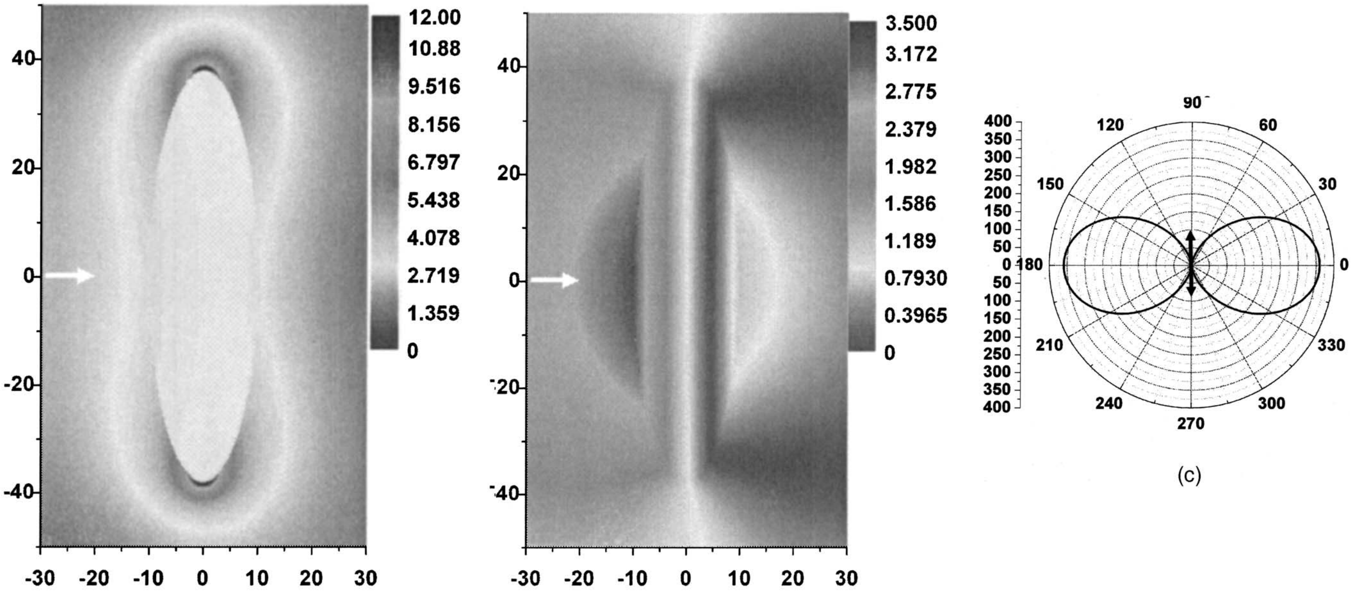

(a) (b) (c)

Fig. 4. Field distribution of the total field of Fig. 2. (a) The total electric field distribution. (b) The total magnetic field distribution. (c) Far-field SCS. The length scale is in nanometers for the x and y-axes. $\bar{\sigma}=176.4$ nm.

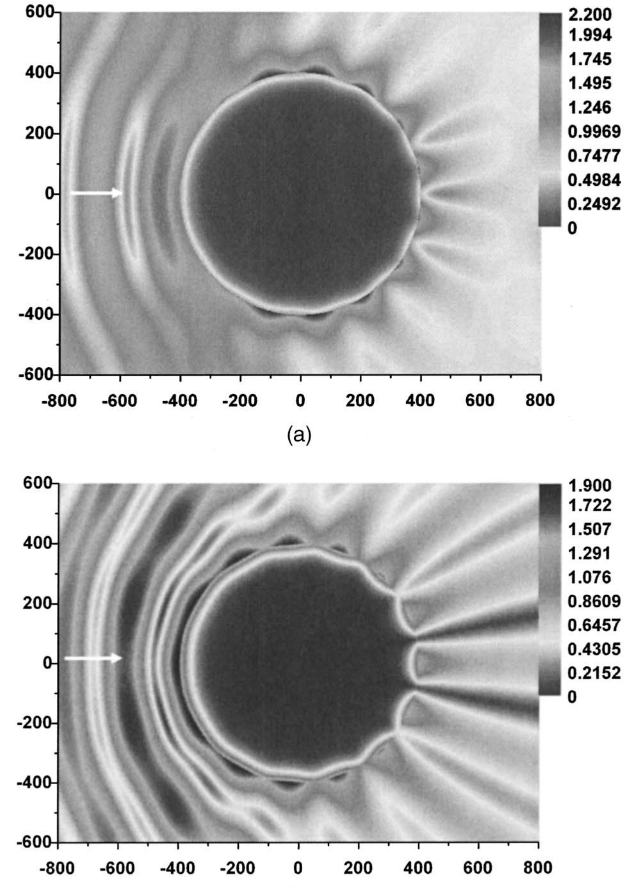

(a)

(b)

Fig. 5. Submicrometer-sized circular silver ($r=400$ nm) with $\epsilon_{2r}=(-4.42,0.73)$, in air, $\epsilon_{1r}=1$, at $\omega=4.558\times10^{15}$ rad/s (3 eV, $\lambda_0=413$ nm) $\theta_i=0°$. (a) The total electric field distribution. (b) The total magnetic field distribution. The length scale is in nanometers for the x and y axes. $\bar{\sigma}=2136$ nm.

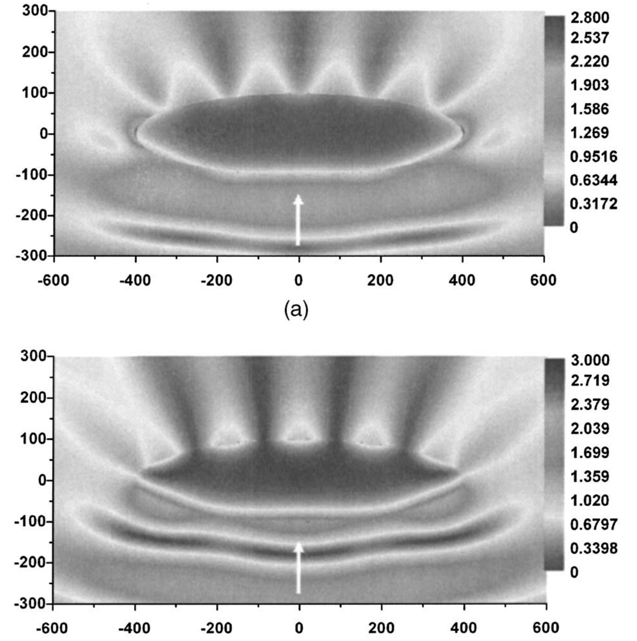

(a)

(b)

Fig. 6. Submicrometer-sized elliptical silver ($a=400$ nm, $b=100$ nm) with $\epsilon_{2r}=(-4.42,0.73)$, in air, $\epsilon_{1r}=1$, at $\omega=4.558\times10^{15}$ rad/s (3 eV), $\theta_i=90°$. (a) The total electric field distribution. (b) The total magnetic field distribution. The length scale is in nanometers for the x and y axes. $\bar{\sigma}=1648$ nm.

wave at the interface of a half-plane metal and a half-plane dielectric (two semi-infinite domains). Because of the influence of the imaginary part of ϵ_{2r}, the attenuation of the surface plasmon wave is associated with the propagation along the interface. Normally as a surface wave propagating along the interface, the energy is confined to the neighborhood of the interface, and the amplitude of

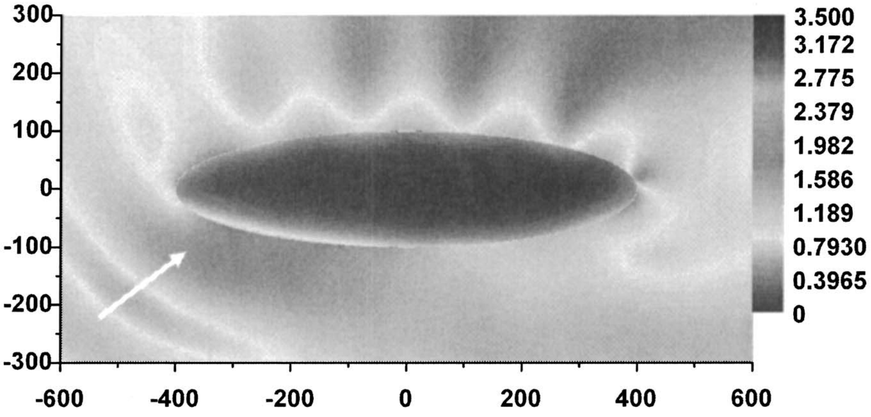

Fig. 7. Total electric field distribution of an elliptical silver ($a=400$ nm, $b=100$ nm) in air, $\epsilon_{1r}=1$, at $\omega=4.558\times10^{15}$ rad/s (3 eV), $\theta_i=45°$. The length scale is in nanometers for the x and y axes. $\bar{\sigma}=599$ nm.

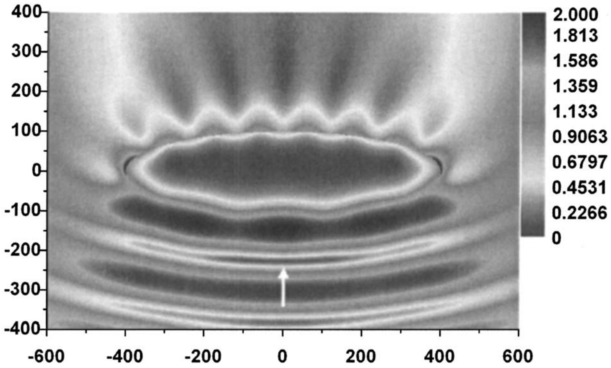

Fig. 8. Total electric field distribution of an elliptical silver ($a=400$ nm, $b=100$ nm) in water, $\epsilon_{1r}=1.777$, at $\omega=4.558\times10^{15}$ rad/s (3 eV), $\theta_i=90°$. The length scale is in nanometers for the x and y axes. $\bar{\sigma}=1608$ nm.

the field decays exponentially with the distance from the interface, like an evanescent wave. The decay constants γ_1 and γ_2 of the surface plasmon wave in the dielectric and the metal are

$$\gamma_1{}^2 = -k_0{}^2 \frac{\epsilon_{1r}^2}{\epsilon_{1r}+\epsilon_{2r}}, \quad \gamma_2{}^2 = -k_0{}^2 \frac{\epsilon_{2r}^2}{\epsilon_{1r}+\epsilon_{2r}}. \tag{40}$$

Hence the penetration depth of the surface plasmon wave of Eqs. (40) in dielectric is $1/\mathrm{Re}(\gamma_1)$ and in metal it is $1/\mathrm{Re}(\gamma_2)$. For the case $\epsilon_{2r}=(-4.42, 0.73)$, $\epsilon_{1r}=1$, at $\omega=4.558\times10^{15}$ rad/s (3 eV), the penetration depth estimated by Eqs. (40) is 123.7 nm in dielectric and is 27.5 nm in silver. As shown in Fig. 5, the electric and magnetic fields inside the metallic scatterer are zero except at a skin zone near the interface because the penetration depth of the surface plasmon wave is much smaller than the characteristic length, i.e., the shielding effect causes a null field inside the metal. Taking account of the geometric effect, convex or concave, the attenuation of the surface plasmon wave increases, i.e., a certain amount of energy radiates into the surrounding medium, as the wave creeps along a curve surface. In addition, the speed of the surface plasmon wave along a curve is slower than that predicted by Eq. (39) for a flat plane. Generally, the behavior of the creeping surface plasmon wave along a curve is more complicated than that of Eq. (39), which is a special case with an infinite radius. Nevertheless, Eqs. (39) and (40) are still useful to describe the main features of the surface plasmon wave on a submicrometer structure. In Fig. 5 the pitch of the nodal points is around 164 nm (along the curve), which is close to a half of the wavelength, $\lambda_{\mathrm{sp}}=365$ nm, predicted by Eq. (39). Subsequently, we consider an elliptical silver ($a=400$ nm, $b=100$ nm), in air, $\epsilon_{1r}=1$ (3 eV, $\lambda_0=413$ nm). From the distributions of the electric and magnetic fields, ripples of corona with nodal points along the backside contour of the scatterer are also observed in Fig. 6 with $\theta_i=90°$ and in Fig. 7 with $\theta_i=45°$. The former is a symmetric case, and the latter is a nonsymmetric one. The numerical results illustrate that the standing wave always exists no matter whether the geometric configuration is symmetric or not. We also consider the effect of the surrounding medium by embedding the elliptical silver in an aqueous solution, $\epsilon_{1r}=1.777$, at $\omega=4.558\times10^{15}$ rad/s (3 eV). The electric field distribution is plotted in Fig. 8. The same phenomenon is also observed as for the cases in air. However, when the size of the metallic particle becomes larger, say 1 μm, the standing wave no longer exists because the two opposite-direction plasmon waves are attenuated to vanish before they can interfere with each other.

Normally it is more difficult to implement the calculation for a larger scatterer than for a smaller one by using the numerical methods that need a domain mesh. In contrast, the surface integral equations solved by the BEM have some advantages since only the boundary of the scatterer needs to be meshed and the Green's functions automatically satisfy the far-field radiation condition. In particular, when a multiscattering problem with different orders of the sizes of the scatterers is dealt with, the boundary mesh is easier to implement and takes less memory than the domain mesh.

6. CONCLUSIONS

The capability of the new surface integral equations was demonstrated on the SPR of nanometer- and submicrometer-sized structures of circular and elliptical metals by the BEM. For the nanometer-sized cases (dimension of tens of nanometers), the numerical results confirm that the near-field enhancement of the electric field can be strong, if the resonance condition is met, and the corresponding pattern of the far-field SCS is like a dipole. For the submicrometer-sized cases (dimension of several hundreds of nanometers), the numerical results point out the existence of a standing wave on the surface of the metals caused by two surface plasmon waves creeping along the contour of metals clockwise and counterclockwise, creating an interference on the backside of the scatterer. Even though we change the permittivity of the surrounding medium and the aspect ratio of the particle's shape, the standing waves always exist. The standing waves, regarded as nanoantennas or gratings, could generate a unique forward scattering. This novel phenomena could be utilized to manipulate the incident light for special purposes. However, the near-field enhancement of the electric field of the submicrometer-sized structure is less compared with that of the nanometer-sized one.

ACKNOWLEDGMENTS

The author thanks J.-K. Wang and M.-K. Kuo, National Taiwan University, for helpful discussions. This research was supported by the Ministry of Economic Affairs through the Industrial Technology Research Institute in Taiwan, Republic of China (grant A321XS9L10). J.-W. Liaw's e-mail address is markliaw@mail.cgu.edu.tw. His present address is Department of Mechanical Engineering, Chang Gung University, 259 Wen-Hwa 1st Road, Kwei-Shan, Tao-Yuan, 333 Taiwan.

REFERENCES

1. T. W. Ebbesen, H. J. Lezec, H. F. Ghaemi, T. Thio, and P. A. Wolff, "Extraordinary optical transmission through sub-wavelength hole arrays," Nature **391**, 667–669 (1998).
2. L. B. Blanco and F. J. Garcia de Abajo, "Spontaneous emission enhancement near nanoparticles," J. Quant. Spectrosc. Radiat. Transf. **89**, 37–42 (2004).
3. H. Xu, J. Aizpurua, M. Kall, and P. Apell, "Electromagnetic contributions to single-molecule sensitivity in surface-enhanced Raman scattering," Phys. Rev. E **62**, 4318–4324 (2000).
4. F. J. Garcia de Abajo, "Light transmission through a single cylindrical hole in a metallic film," Opt. Express **10**, 1475–1484 (2002).
5. L. B. Yu, D. Z. Lin, Y. C. Chen, Y. C. Chang, K. T. Huang, J. W. Liaw, J. T. Yeh, J. M. Liu, C. S. Yeh, and C. K. Lee, "Physical origin of directional beaming emitted from a subwavelength slit," Phys. Rev. B **71**, 041405(R) (2005).
6. G. Schider, J. R. Krenn, A. Hohenau, H. Ditlbacher, A. Leitner, F. R. Aussenegg, W. L. Schaich, I. Puscasu, B. Monacelli, and G. Boreman, "Plasmon dispersion relation of Au and Ag nanowires," Phys. Rev. B **68**, 155427 (2003).
7. J.-C. Weeber, A. Dereux, C. Girard, G. C. des Francs, J. R. Krenn, and J.-P. Goudonnet, "Optical addressing at the subwavelength scale," Phys. Rev. E **62**, 7381–7388 (2000).
8. J. W. Liaw and J. K. Wang, "Dispersion relation of plasmon wave in metallic nanowires," Scanning Microsc. **26**, 106–108 (2004).
9. S. A. Maier, P. G. Kik, and H. A. Atwater, "Optical pulse propagation in metal nanoparticle chain waveguides," Phys. Rev. B **67**, 205402 (2003).
10. V. A. Podolskiy, A. K. Sarychev, and V. M. Shalaev, "Plasmon modes in metal nanowires and left-handed materials," J. Nonlinear Opt. Phys. Mater. **11**, 65–74 (2002).
11. J. P. Kottmann, J. F. Martin, D. R. Smith, and S. Schultz, "Spectral response of plasmon resonant nanoparticles with a non-regular shape," Opt. Express **6**, 213–219 (2000).
12. J. P. Kottmann and J. F. Martin, "Plasmon resonant coupling in metallic nanowires," Opt. Express **8**, 655–663 (2001).
13. J. P. Kottmann, J. F. Martin, D. R. Smith, and S. Schultz, "Plasmon resonances of silver nanowires with a nonregular cross section," Phys. Rev. B **64**, 235402 (2001).
14. E. Moreno, D. Erni, C. Hafner, and R. Vahldieck, "Multiple multipole method with automatic multipole setting applied to the simulation of surface plasmons in metallic nanostructures," J. Opt. Soc. Am. A **19**, 101–111 (2002).
15. C. Rockstuhl, M. G. Salt, and H. P. Herzig, "Application of the boundary-element method to the interaction of light with single and coupled metallic nanoparticles," J. Opt. Soc. Am. A **20**, 1969–1973 (2003).
16. F. J. Garcia de Abajo and A. Howie, "Retarded field calculation of electron energy loss in inhomogeneous dielectrics," Phys. Rev. B **65**, 115418 (2002).
17. C. I. Valencia, E. R. Mendez, and B. S. Mendoza, "Second-harmonic generation in the scattering of light by two-dimensional particles," J. Opt. Soc. Am. B **20**, 2150–2161 (2003).
18. A. Stratton, *Electromagnetic Theory* (McGraw-Hill, 1941), pp. 464–467.
19. K. Tanaka, M. Tanaka, and K. Katayama, "Simulations of two-dimensional photon scanning tunneling microscope by boundary integral equation method: p-polarization," Opt. Rev. **6**, 249–256 (1999).
20. D. W. Prather, J. N. Mait, M. S. Mirotznik, and J. P. Collins, "Vector-based synthesis of finite aperiodic subwavelength diffractive optical elements," J. Opt. Soc. Am. A **15**, 1599–1607 (1998).
21. L. Rogobete and C. Henkel, "Spontaneous emission in a subwavelength environment characterized by boundary integral equations," Phys. Rev. A **70**, 063815 (2004).
22. M. K. Choi, "Numerical calculation of light scattering from a layered sphere by the boundary-element method," J. Opt. Soc. Am. A **18**, 577–583 (2001).
23. J. W. Liaw, S. L. Chu, C. S. Yeh, and M. K. Kuo, "Analysis of eddy current in a bar containing an embedded defect," NDT & E Int. **32**, 293–303 (1999).
24. E. D. Palik, *Handbook of Optical Constants of Solids* (Academic, 1985).